Chrysalis-Like Graphene Oxide Decorated Vanadium-Based Nanoparticles: An Extremely High-Power Cathode for Magnesium Secondary Batteries

Journal of The Electrochemical Society, 2020 **167** 070547

Chrysalis-Like Graphene Oxide Decorated Vanadium-Based Nanoparticles: An Extremely High-Power Cathode for Magnesium Secondary Batteries

Gioele Pagot,[1,2,*] Keti Vezzù,[1,3,*] Angeloclaudio Nale,[1,*] Maurizio Fauri,[4] Andrea Migliori,[5] Vittorio Morandi,[5] Enrico Negro,[1,2,3] and Vito Di Noto[1,2,3,*,,z]**

[1]*Section of Chemistry for the Technology (ChemTech), Department of Industrial Engineering, University of Padova, I-35131 Padova (PD), Italy*
[2]*Centro Studi di Economia e Tecnica dell'Energia Giorgio Levi Cases, I-35131 Padova (PD), Italy*
[3]*INSTM, I-35131 Padova (PD), Italy*
[4]*Department of Civil, Environmental and Mechanical Engineering, University of Trento, I-38123 Trento (TN), Italy*
[5]*National Research Council of Italy, Institute for Microelectronics and Microsystems—CNR IMM section of Bologna, I-40129 Bologna (BO), Italy*

Rechargeable batteries based on magnesium virtually provide high volumetric capacity, safety, and cost savings thanks to the abundance, dendrite-free electrodeposition, and environmentally green properties of Mg metal anode. The lack of cathodes that can deliver high currents at high potential is one of the principal bottlenecks that limit the entrance of Mg batteries into the market. Here we report the synthesis and characterization of a novel cathode for magnesium secondary batteries based on graphene oxide (GO) and vanadium (V) active species. Thermogravimetric analysis, structural and vibrational analyses, and high-resolution electron microscopies elucidate the complex architecture that characterizes the proposed material and that bestows exceptional electrochemical properties to the cathode. The proposed synthesis is able to give rise to V-based nanoparticles with a very porous surface and wrapped inside a chrysalis-like GO ordered superstructure. Finally, a coin cell device is assembled using a Mg metal anode and the proposed material as cathode. This prototype is able to deliver good capacities when cycled at high current rates (1000 mA g^{-1}) in a higher potential range with respect to classical cathodes for Mg batteries. Thus, a sufficient power (1.70 W g^{-1}) is obtained, making this battery promising towards the substitution of lithium batteries.
 [DOI: 10.1149/1945-7111/ab7fb4]

Manuscript submitted December 9, 2019; revised manuscript received February 20, 2020. Published March 30, 2020. *This paper is part of the JES Focus Issue on Challenges in Novel Electrolytes, Organic Materials, and Innovative Chemistries for Batteries in Honor of Michel Armand.*

Supplementary material for this article is available online

Lithium-ion batteries are currently considered the best high-performance rechargeable electrochemical power source, dominating the world market of electrical applications (e.g., portable electronic devices, light-duty vehicles).[1,2] However, lithium is a strategic metal and its resources are located only in a few countries, making Li cost very high and raising concerns about the occurrence of supply bottlenecks.[3] Furthermore, lithium metal is inherently unstable and presents health, safety, and environmental issues. Following these issues, the research has been focused on the development of new secondary battery systems with fewer drawbacks and exhibiting a performance comparable to that of lithium-based devices. Magnesium-ion batteries are a valid alternative to lithium-ion batteries in order to overcome several of the disadvantages presented by lithium. With respect to lithium, Mg is: a) much more abundant; b) more than 20 times cheaper; c) is environmentally green; d) can be safely handled in air; e) shows a dendrite-free electrodeposition; and f) has an intrinsic higher theoretical volumetric capacity (3833 mAh cm^{-3} vs 2046 mAh cm^{-3} of lithium).[4] Great efforts have been devoted in order to develop high-performing electrolytes for the efficient deposition and stripping processes of magnesium at the anode,[5–15] and high-capacity and high-energy cathode materials.[16–23] The Chevrel-phase (Mo_6S_8) is today the state of the art in cathode materials owing to its remarkable specific capacity and durability, even though this cathode exhibits an average discharge voltage centered at ca. 1.20 V vs Mg/Mg^{2+}. Unfortunately, no results are reported in the literature on cells cycling this cathode material at current rates higher than 500 mA g^{-1}.[24] A rare example of cathode materials cycled at such high current rates consists of a CuS-based conversion cathode.[25] Thus, both the operating voltage and the specific current density need to be increased in order to perform high-power loads and make magnesium batteries an attractive alternative to lithium in the field of rechargeable batteries. It was demonstrated that vanadium-based cathode materials fulfill the above requirements owing to their higher operating voltage (ca. 2.0 V vs Mg/Mg^{2+}) and good specific capacity.[26] The reversible insertion and diffusion of Mg ions in vanadium cathodic active material can be improved by an appropriate functionalization of the surface of the cathode nanoparticles. Consequently, the maximum operating current rate of this material can be significantly increased. Graphene (G) and graphene oxide (GO) are two of the most studied two-dimensional compounds for the functionalization of electroactive materials. They consist of 2D one atom thick conducting flakes which present a high chemical stability, a large surface area, a good mechanical strength and significant flexibility. The above discussed physico-chemical properties make these materials an ideal substrate able to anchor chemically the active nanoparticles, providing the necessary conductivity for their operation. GO surface is characterized on the basal planes and edges by the presence of oxygen functional groups such as hydroxyl, epoxide, carbonyl, and carboxyl groups. These functionalities are able to better fix GO flakes on the surface of vanadium-based species by electrostatic interactions.[27]

Here a cathode material (GO@V) consisting of graphene oxide (GO) decorating vanadium(V)-based nanoparticles is prepared by solvo-thermal synthesis. This material is obtained by reacting suitable vanadium oxychloride and oxysulfate solutions, which are synthetized by following an appropriate electrochemical activation process (see below), with GO flakes. The aim is to study the effect of the interactions between GO flakes and vanadium active species on

*Electrochemical Society Member.
**Electrochemical Society Fellow.
[z]E-mail: vito.dinoto@unipd.it

the electrochemical performance of a single cell. In details, thermal analysis, vibrational studies, and electron microscopy (HR-TGA, ATR-FTIR, confocal micro-Raman, and STEM microscopy) are carried out to investigate the interactions occurring between V and GO. Finally, cyclic voltammetry and battery testing studies are performed to reveal their properties and the electrochemical behavior under charging and discharging processes.

Experimental

Chemicals.—Vanadium(IV) oxide sulfate hydrate (99.9%) ($VOSO_4 \cdot xH_2O$) and graphite (SK6) were purchased from Alfa Aesar and TIMCAL, respectively. Sulfuric acid (98.0%), barium chloride (99.9%), ammonium hydroxide solution (30.0%), polyvinyl difluoride (PVDF), 1-methyl-2-pyrrolidone (NMP, 99.5%, anhydrous), 1-ethyl-3-methylimidazolium chloride-aluminum chloride 1:1.5 ($EMImCl/(AlCl_3)_{1.5}$ ionic liquid, IL), magnesium powder, magnesium foil, vanadium(V) oxide (V_2O_5) and 1-chlorobutane were obtained from Sigma-Aldrich and used as received. Graphene oxide (GO) was home-made produced by the modified Hummers method.[28]

Electrochemical activation of vanadium species.—1.0 M vanadium oxide sulfate solution is prepared by dissolving an appropriate amount (39.12 g) of $VOSO_4$ into 240 mL of a 5.0 M H_2SO_4 water solution. The obtained vanadium solution is divided into two aliquots, with a 1:2 volume ratio. The two solutions are set in two electrochemical semi-cells ionically separated by a Nafion 117® proton conducting membrane. Then, a carbon paper electrode is dipped into the solution of each semi-cell. A potential difference of +1.80 V is applied between the two electrodes. The electrochemical activation process of the two solutions is completed when in the negative side of the system the oxidation of V(IV) to V(V) species achieves a yield of ca. 96%. Concurrently, in the positive semi-cell, V(II) species are obtained. All the here described operations are carried out under an Ar inert atmosphere.

Synthesis of GO@V.—60 mL of the 1.0 M V(V) oxide sulfate, electrochemically obtained as previously described, are diluted in a 500 mL volume flask by adding 240 mL of double-distilled water. Subsequently, in order to eliminate sulfuric acid from the mixture, 62.64 g of barium chloride is added to this vanadium solution, forming a white precipitate of $BaSO_4$. The heterogeneous mixture is stirred for 2 h and then filtered. 5 mL of a GO suspension in water (10 mg mL^{-1}) is added to 100 mL of the filtered vanadium solution, and the mixture is vigorously stirred for 30 min. Subsequently, 4.5 mL of a 30% NH_4OH aqueous solution is added dropwise to the mixture and stirred for 1 h. The obtained mixture is transferred into a Teflon beaker inserted into a stainless-steel autoclave. After sealing, the autoclave is heated at 2 °C min^{-1} up to 200 °C and maintained at this temperature for 12 h. After cooling, the resulting mixture is dried under vacuum (10^{-2} mbar) at 90 °C overnight. A brown solid of GO@V is obtained, which is extensively washed with cold methanol. Finally, the resulting GO@V material is dried under vacuum (10^{-2} mbar) at 70 °C for 12 h.

Chemical and structural characterizations.—The nominal composition of GO@V sample is determined by Inductively Coupled Plasma Optical Emission Spectroscopy (ICP-OES) and CHNS elemental analysis measurements. The solution to carry out the ICP-OES analyses is obtained by digesting the sample in an acidic water solution consisting of a 3:1 mixture of HCl and HNO_3. The emission lines of V and Ba are 292.646 and 455.404 nm, respectively. High Resolution-Thermogravimetric Analyses (HR-TGA) are carried out by using a high-resolution thermobalance (2950 model of TA Instruments). Mass losses are evaluated in the temperature range from 30 °C to 950 °C under a N_2 atmosphere. The heating rate is modulated in the range 50 ÷ 0.001 °C min^{-1} on the basis of the first derivative of the weight loss. The instrumental sensitivity ranges from 0.1 to 2% min^{-1} and the weight resolution is ca.1 μg. The morphology of the sample is investigated by Scanning Electron Microscopy (SEM) (model JSM Jeol 6490). Microstructure is determined with a high-resolution transmission electron microscope at 200 keV with a TEM/STEM FEI TECNAI F20 mounting a high-angle collecting annular detector. The medium-infrared spectrum is collected using a Thermo Scientific spectrometer (model Nicolet Nexus) and a SPECAC Golden Gate single reflection diamond ATR cell. The final spectrum with a resolution of 2 cm^{-1} is obtained by averaging 500 scans. Micro-Raman profiles are measured by means of a confocal DXR-Micro Raman (Thermo Scientific) spectrometer with a 532 nm excitation line laser. Wide-angle powder X-ray diffraction measurements of the pristine and fully discharged materials are measured with a GNR analytical instrument (mod. eXplorer) with a Cu K_α source in the 2θ range 5°–60° with a 0.04° step and an integration time of 40 and 120 s, respectively. Lattice parameters for GO@V are calculated using the Rietveld method with Maud software.[29] Refinements are conducted starting from the structure of an ammonium chloroferrate phase (available in the Crystallography Open Database (COD), http://crystallography.net/, COD ID 9012597) in which iron is substituted by vanadium ions. Structural parameters are calculated minimizing the weighted profile R-factor, up to R_{wp} 5.99%.

Electrochemistry.—The synthesized GO@V material is used to prepare a cathode electrode as described below. Its electrochemical performance is evaluated by both cyclic voltammetry (CV) measurements and battery cycling processes in a single full cell CR2032 device including a magnesium metal anode and a suitable electrolyte. To prepare the cathode, the active material is mixed with SK6 and PVDF in a weight ratio 45.5:51.0:3.5 and then suspended in NMP. The resulting slurry is coated directly on a platinum foil, with a mass loading of 0.9 mg cm^{-2} for CV measurements, or alternatively for single-cell studies on the case of a CR2032 coin cell, with an average mass loading of 1.8 mg cm^{-2}. CV measurements are carried out adopting the typical three-electrode cell configuration consisting of a working electrode based on a Pt foil coated with the cathodic material, a magnesium ribbon reference electrode, and a magnesium foil counter electrode. This electrochemical cell is assembled and operated inside an argon-filled glove-box. The CR2032 coin cell device is sealed under an inert Ar atmosphere in the same conditions by using a magnesium metal foil as anode and a glass fiber separator. The electrolyte used in both the CV measurements and the battery tests is a solution obtained by dissolving 2 wt% of δ-$MgCl_2$ into the $EMImCl/(AlCl_3)_{1.5}$ ionic liquid.[5] δ-$MgCl_2$ salt is a particularly active form of magnesium chloride, which is characterized by a very high crystallographic disorder and reactivity. It is obtained by a direct reaction of magnesium powder with 1-chlorobutane following a well-known procedure.[8–10,30] For the sake of comparison, pristine V_2O_5 is used as reference material to prepare a cathodic mixture and to study its electrochemical performance in a battery prototype. The CV profiles are measured at different scan rates (from 5 to 100 mV s^{-1}) in the potential range 0.5 ÷ 2.5 V. The CR2032 single-cell is cycled in a potential range from 0.5 V to 2.5 V by applying a galvanostatic procedure at a current rate of 1000 mA g^{-1} (i.e. 4.12 mA cm^{-2}), corresponding to ca. 12.5 C, using a battery tester (MACCOR model 2300). Fully discharged GO@V sample for structural characterizations is obtained by disassembling the discharged battery inside an Ar-filled glove-box. The cathode electrode here recovered is then thoroughly washed with anhydrous 1-propanol in order to remove any electrolyte traces.

Results and Discussion

The material here proposed is the result of a very well-designed synthetic protocol developed into this work (see Scheme 1) which allows to obtain cathode materials with an appropriate architecture. This morphology allows to improve the magnesium ion transfer at the electrolyte-cathode material interface and its intrinsic red-ox kinetics during charge-discharge processes.

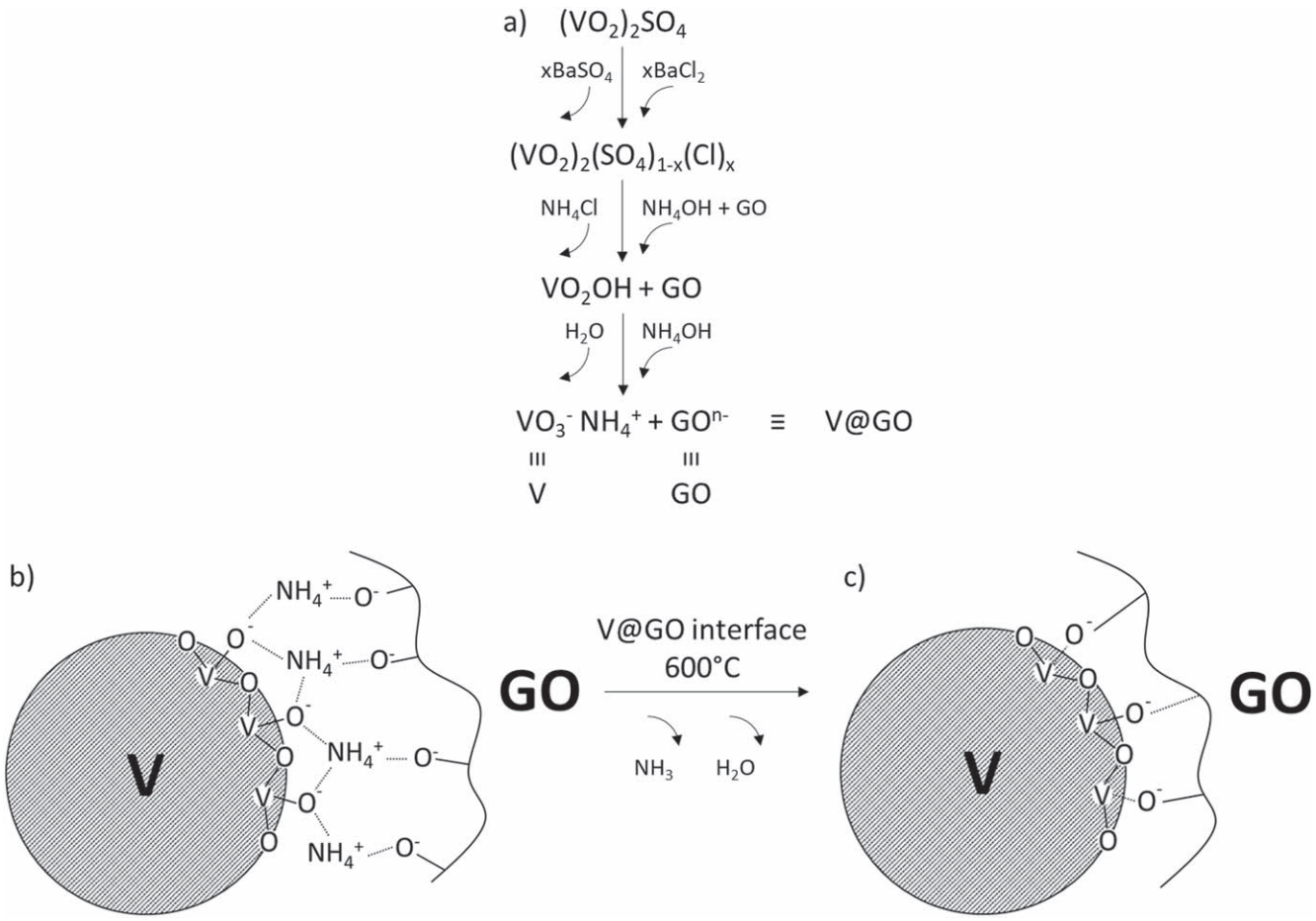

Scheme 1. Reaction pathway on the surface of V nanoparticles (a). Possible electrostatic interactions at the VO_3^-/GO^{n-} interface (b). Binding interactions at the interface VO_3^-/GO^{n-} after pyrolysis at 600 °C carried out under N_2 during the HR-TGA analysis (c).

Stoichiometry of cathodic material.—ICP-OES and CHNS analyses demonstrate that GO@V material consists of vanadium and GO with a weight ratio of 20:1. This vanadium/carbon weight ratio is the best compromise to obtain the desired architecture where graphene oxide flakes are mainly covering the surface of vanadium-based nanoparticles (V-NPs), thus improving their interactions, mechanical properties, and facilitating their electronic contact with the electrode (conductivity of cathodic material). Elemental analysis reveals the presence of nitrogen, corroborating the hypothesis that a positively charged ammonium inter-layer is present, which is sandwiched between V-NPs and GO and which facilitates the interactions between the vanadium "*core*" nanoparticles and the GO flakes through electrostatic interactions (Scheme 1b). Figure 1a schematically represents the hypothesized architecture of the proposed material. This is a schematic drawing which highlights the main information determined in the proposed material by the morphology, structure and spectroscopic studies. Less than 0.1 wt % of barium is found, confirming that the formed $BaSO_4$ is completely eliminated during the washing/filtering process.

Thermal stability.—The results of the investigations carried out by high-resolution thermogravimetry (HR-TGA) are shown in Fig. 1b. Three main events are revealed in the HR-TGA profile at ca. 150 °C, 250 °C, and 460 °C. These thermal events are the result of a progressive degradation of the ammonium electrostatic layer, with the consequent formation in the electrostatic interface of different types of ammonium-oxyvanadyl species.[31] The elimination of chlorine- and sulphur-based species during the ammonium thermal decomposition cannot be excluded. At 315 °C a slight weight loss is observed, that can be attributed to the decomposition of traces of ammonium chloride species which were not eliminated during the reactions shown in Scheme 1a. At $T > 600$ °C a residual weight of 27.5 wt% is detected, which corresponds to a material formed owing to the direct interaction between vanadium oxide-based nanoparticles and graphene oxide material as depicted in Scheme 1c.

The HR-TGA profile is crucial in order to reveal the composition of the active material. Indeed, this profile is perfectly coherent with that corresponding to the thermal degradation of ammonium metavanadate, which, as elsewhere described,[31] occurs into a three step process: $NH_4VO_3 \rightarrow (NH_4)_2V_4O_{11} \rightarrow NH_4V_3O_8 \rightarrow V_2O_5$ at 160 °C, 195 °C, and 260 °C, respectively. Differently from NH_4VO_3, in the proposed GO@V the ammonium decomposition and elimination process (see Scheme 1c) is shifted towards higher temperatures, thus indicating that: i) the electrostatic interactions at the interface VO_3^-/GO^{n-} act to thermally stabilize the obtained materials; and ii) the surface of GO nanoflakes, with alkoxide oxygen functionalities, interact strongly with the NH_4^+ ions of the ammonium layer bridging the oxyvanadyl-based nanoparticles. Thus, a strong interaction network at the interface VO_3^-/GO^{n-} is formed, which stabilizes the proposed architecture.

Morphology and structure.—The SEM and STEM micrographs of the GO@V composite are shown in Fig. 2.

From SEM images it can be seen that a homogeneous dispersion of particle aggregates is obtained. In details, a bi-modal particle size distribution is detected by SEM images: i) the first consists of larger aggregates exhibiting an average diameter of ca. 5 μm; ii) the second includes smaller particles with an average diameter of ca. 1 μm, which are supported on the surface of larger particle agglomerates.

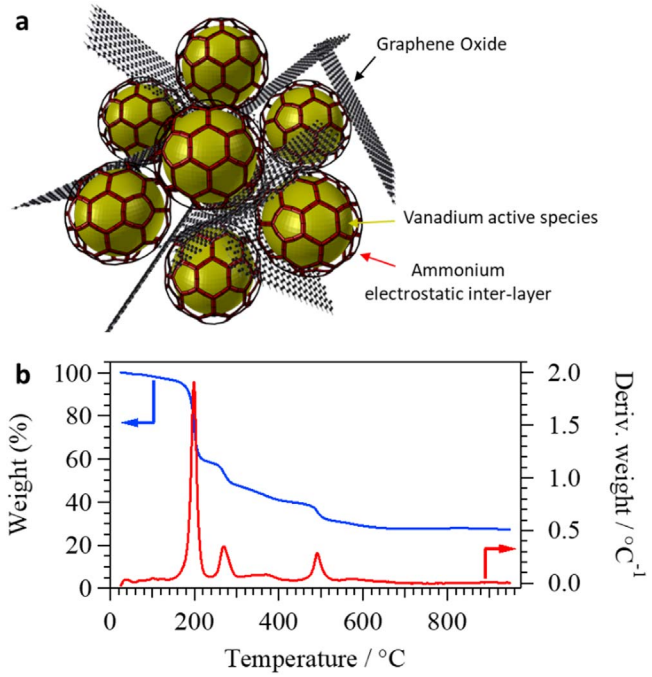

Figure 1. Representative sketch of the GO@V architecture (a). A hypothesis on the distribution of the positively-charged ammonium bridging inter-layer is shown. The possible electrostatic interactions at the VO_3^-/GO^{n-} interface is shown in Scheme 1b. This sketch is just a conceptual drawing. Size and shape of the components may differ from the real sample. HR-TGA profiles of GO@V is measured under a N_2 atmosphere (b).

Scanning Transmission Electron Microscopy (STEM) images (Figs. 2c–2f) definitively confirm the above hypothesized architecture for the proposed material and show in details how the components of GO@V sample are embedded together. GO nanoflakes are homogeneously wrapping the vanadium-based nanoparticles on their surfaces in a sort of *chrysalis-like* ordered superstructure. All the analyzed nanoparticles show the presence of a very porous layer between the GO nanoflakes and the vanadium-based component (see d and e panels of Fig. 2). This layer is reasonably attributed to the ammonium ion bridges that bond together GO and V components through electrostatic interactions. Thus, the above hypothesized representative sketch of the GO@V architecture (Fig. 1a) is confirmed by STEM images. EDX mapping confirms that GO@V nanoparticles are composed by a mixture of vanadium, sulfur, and chlorine atoms, together with nitrogen and carbon which are composing the ammonium inter-layer and the GO nanoflakes, respectively.

Further insights on the structure and on the interaction framework existing in GO@V sample can be obtained by both Raman and ATR FT-IR vibrational spectroscopy investigations (see Fig. 3).

The ATR FT-IR and micro-Raman spectra can be factorized into three different diagnostic regions, I, II, and III, which are correlatively assigned as summarized in Table I. In region I, from 4000 to 1850 cm^{-1}, the presence of the typical −NH, −CH, and −OH stretching modes is revealed, which are arising from the graphene oxide flakes and the ammonium bridges (see Scheme 1b).[32–42] In region II (1850 ÷ 1050 cm^{-1}), the typical bending modes of ammonium ions can be detected at around 1390 and 1710 cm^{-1} for the antisymmetrical (ν_4) and symmetrical (ν_2) vibrations, respectively.[38–42] At ca. 1760 and 1540 cm^{-1} bands attributed to the combination of ν_4 mode to rotational lattice modes of ammonium ion are determined.[38–42] Finally, several other peaks which are attributed to the GO matrix are present in the vibrational spectra.[32,33,35,36,43–46] In the last region (III), below 1050 cm^{-1}, the peaks are assigned to the vibrational modes of different V–X ($X = -O^-NH_4^+$, SO_4^{2-}, Cl^-) functional groups[31,37,47–50] and of a rotational lattice mode of the ammonium ions[38–42] (see Table I).

Ammonium ions ($P_{4/nmm}$ crystal structure with a D_{2d}-site symmetry and a D_{4h} factor group symmetry)[51] are useful probes in solid state to investigate in details the interactions arising between the different components composing GO@V sample. Thus, the assignment and discussion of vibrational modes related to the ammonium ions, which are mainly present in region I, is of crucial importance for a correct description of the interaction framework characterizing the proposed material. Ammonium ions have a tetrahedral (T_d) point symmetry with four normal modes of vibration: 1) ν_1 (A_1), which corresponds to the symmetric N–H stretching vibration; 2) ν_2 (E), which is attributed to the symmetric H–N–H bending vibration; 3) ν_3 (F_2), which corresponds to the antisymmetric N–H stretching vibration; and 4) ν_4 (F_2), which is attributed to the antisymmetric H–N–H bending vibration.[38] In addition, the detection of a factor group splitting in the vibrational modes of NH_4^+ demonstrates that ammonium ions are sitting in specific equivalent positions within the crystal unit cell, giving so rise to *correlation effects* which provide information on the type of structure of this system.[52,53] In details, these effects are the result of the correlation existing between the vibrational modes of point site symmetry and those in solid-state factor group. Lattice mode vibrations of the ammonium crystal (ν_6, see region II of Fig. 3 and Table I in NH_4Cl reference material), are detected when a polarizability tensor arises from these correlations.[51] In this case it is demonstrated that ν_6 lattice mode is associated to a rotational rather than to a librational motion of the NH_4^+ ions.[41] This rotational mode is not completely free; indeed, ammonium ions cannot rotate freely around the NH_4^+···X-axis in these crystals.[41] Differently from NH_4Cl, ν_6 rotational lattice mode is not detected in GO@V sample (see Fig. 3 and Table I), thus it can be hypothesized that ammonium ions are fixed in their occupation site and cannot rotate in the proposed sample. Likely, they are strongly bridged to both the vanadium-based substrate and to the graphene oxide nano-flakes. The peak position of the ammonium vibrational modes is diagnostic of the strength of the interactions existing between the different components in this cathode. Indeed, in GO@V $\nu(NH_4^+)$ modes are detected all at high wavenumbers with respect to the reference NH_4Cl material. This can be easily explained considering that the N–H···X hydrogen bonds present in the proposed sample are stronger in comparison to those measured in reference NH_4Cl,[38] thus confirming that GO- and V-based components are strongly interacting together by electrostatic forces mediated through ammonium bridges. Furthermore, the spectra of both GO@V sample and the NH_4Cl reference material reveal the presence of combination and overtone bands (see Fig. 3 and Table I). These latter modes, which are involving the ν_6 mode, are detected only for NH_4Cl sample (see Fig. 3 and Table I).

Region II of micro-Raman spectrum is diagnostic of the degree of disorder-order characterizing the graphene oxide component. Indeed, the ratio between the intensity of the D and G bands is widely adopted to evaluate semi-quantitatively the density of defects in the GO component.[54] The G band is attributed to the *in-phase* vibration of the E_{2g} mode of the sp^2 carbon domains,[54] while the D band becomes Raman active when in the graphene oxide matrix: a) a disordered structure with a symmetry breaking is formed[54] or b) defects are present, such as edges on the flakes, surface functionalities, and others. In the proposed cathode, the I_D/I_G ratio is ca. 0.46, where I_D and I_G are the intensities of the peaks attributed to the D and G bands, respectively. As expected, this indicates that in the studied materials a high density of functionalities is present on the surface of the GO component.

The region at low wavenumbers (III), which is mainly associated to the vibrational modes of V-species, is the fingerprint of the complex chemical bonding that characterizes the vanadium-based moiety of GO@V sample. Several vibrational modes are revealed, which are associated to the: a) $(V–O–V)_n$ modes of the concatenated V-clusters characterizing the nanoparticles; b) vanadium-oxysulfide

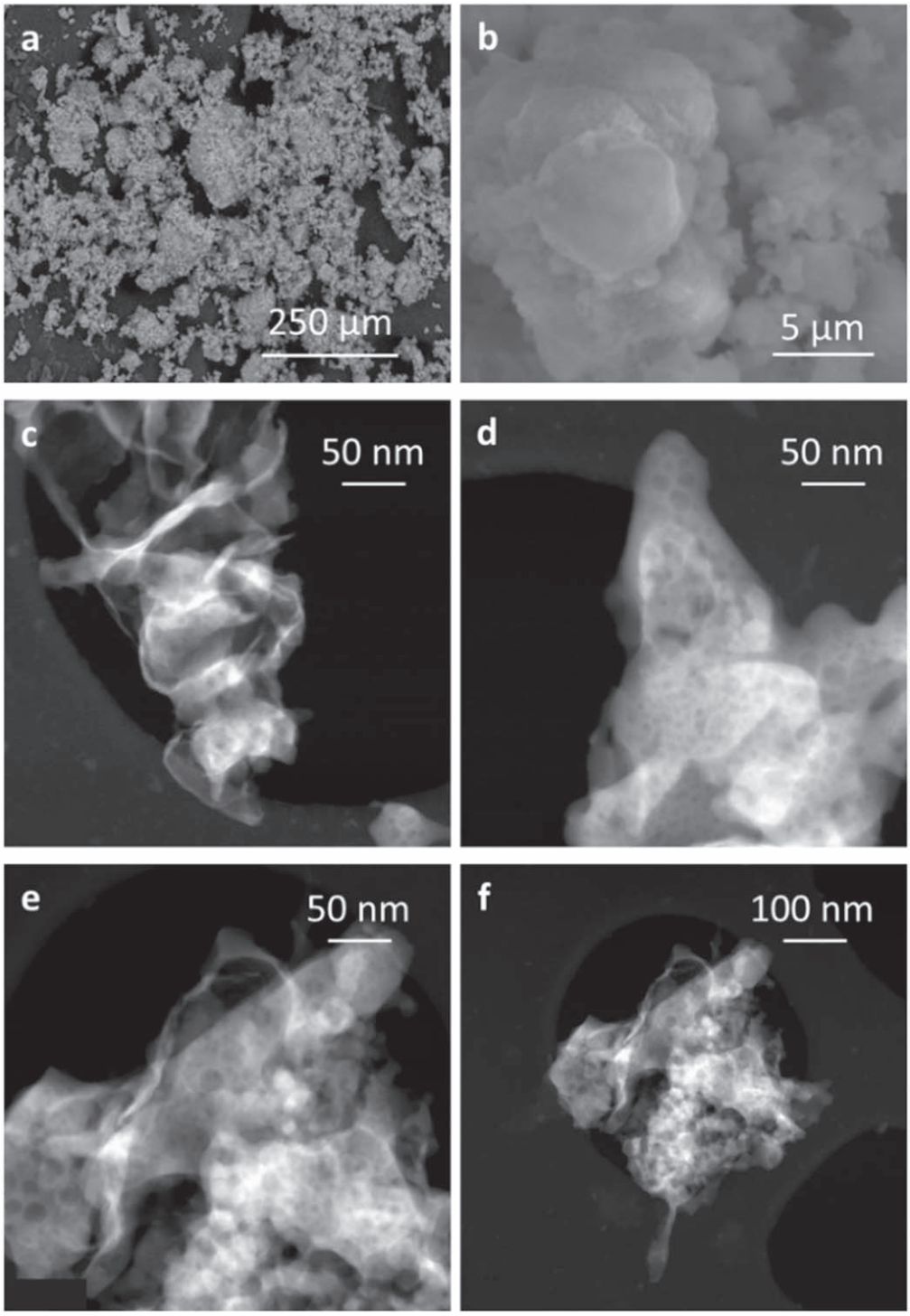

Figure 2. SEM and STEM micrographs of GO@V material at different magnifications and in different regions of the sample (a)–(f).

vibrational modes, which demonstrate that a fraction of sulfate anions are vicariant to oxygen atoms; c) modes associated to oxygen atoms bridging between 3 and 4 vanadium atoms; and d) vibrational modes associated to $(Cl–V–Cl)_n$ bridges. Finally, the peak centered at ca. 663 cm^{-1}, which corresponds to the breathing vibrational mode of a 3D V–O network, suggests that the vanadium-based nanoparticles are predominately consisting of aggregates of V–O complexes concatenated in a 3D framework structure.[47]

The structure of GO@V sample is investigated by the wide-angle powder X-ray diffraction analysis (WAXD) and the spectrum is shown in Fig. 4.

The main V-based phase is isostructural with an analogous ammonium chloroferrate material exhibiting an orthorhombic crystal system with a P n m a (62) space group.[55] Thus, Rietveld analysis is carried out by replacing into its metal structural occupancy sites iron with vanadium ions. Peaks attributed to the reflections of ammonium chloride and graphene oxide phases are also detected at their typical 2theta values.[56–59] The lattice parameters thus determined for V-based nanoparticles are: a = 13.71 Å, b = 9.93 Å and c = 7.04 Å. The average particle size is of ca. 150 nm, which is in agreement with STEM results. This investigation confirms the hypothesis that the material consists of three components (the

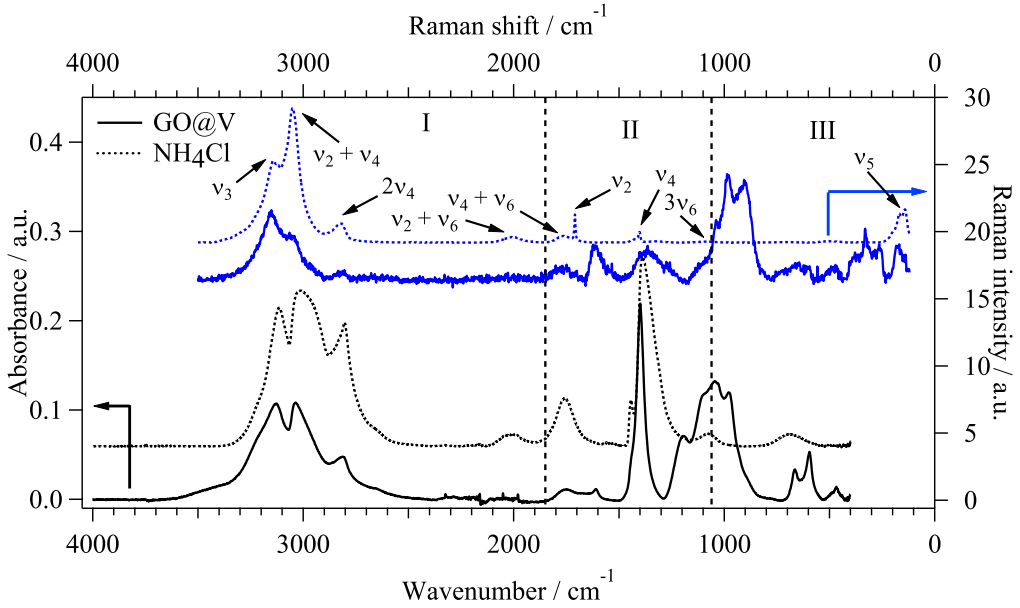

Figure 3. Micro-Raman (blue) and ATR-FTIR (black) vibrational spectra of GO@V (solid lines) and NH_4Cl (dotted lines) samples. NH_4Cl is used as the reference. Vibrational modes attributed to the ammonium ions (ν_i) are shown in the figure.

Table I. Mid- and Far-FT-IR, and micro-Raman vibrational frequencies assignment for GO@V sample and NH_4Cl reference material.

	ATR-FTIR[a)]		Micro-Raman[a)]			
	GO@V	NH_4Cl	GO@V	NH_4Cl	Assignment[b)]	References
Region I	3447 (vw,sh)				ν(OH)	32–34
	3129 (m)	3114 (m)	3151 (m)	3145 (m)	$\nu_3(NH_4^+)$	38–42
	3036 (m)	3016 (m)	3060 (m)	3050 (s)	$\nu_2 + \nu_4(NH_4^+)$	38–42
	2813(w)	2804 (m)	2835 (w)	2819 (w)	$2\nu_4(NH_4^+)$	38–42
		2004 (vw)		2010 (vw)	$\nu_2 + \nu_6(NH_4^+)$	38–42
Region II		1757 (w)		1764 (vw)	$\nu_4 + \nu_6(NH_4^+)$	38–42
	1749 (vw)		1765 (vw)		ν(C=O) of COO^-	32, 35, 43, 44
				1710 (w)	$\nu_2(NH_4^+)$	38–42
	1609 (vw)		1611 (w)		ν(C=C), G band	32, 33, 35, 44
		1539 (vw)			$\nu_4 + \nu_5(NH_4^+)$	38–42
	1451 (w,sh)	1443 (w)		1430(vw) 1402(w)	$\nu_4(NH_4^+)$	38–42
	1398 (s)	1387 (s)	1372 (w)			
			1280 (w)		ν(C=C), D band	45
	1192 (w)				ν_a(C–O)	46
	1096 (m,sh)		1115 (m,sh)		ν_s(C–O)	35, 36
		1075 (vw)			$3\nu_6(NH_4^+)$	38–42
Region III	1044 (m)		1037 (m)		ν(V=O)$_{term}$	31, 47
	978 (m)		978 (s)		ν(V=O)$_{term}$	31, 37,47–49
			904 (s)		ν(V=O)	48
	663 (w)		660 (vw)		ν_a(V–O–V) + ν_a(V–O–S)	31, 47, 48
	595 (m)				$\delta_s(SO_3)$	48
	467 (w)		465 (vw)		ν_a(V–Cl) + δ(V–O–S)$_{bridg}$ + δ(V–O–V)$_{bridg}$	48–50
			372 (w,sh)		ν_s(V–Cl)	50
			329 (w)		δ_s(Cl–V–Cl)	50
			259 (w)		δ_s(Cl–V–Cl) + δ_a(Cl–V–Cl) + δ(V–O)	49, 50
			176 (w)		δ_s(Cl–V–Cl)	50
				169(w) 141(w)	$\nu_5(NH_4^+)$	38–42

a) s = strong, m = medium, w = weak, vw = very weak, sh = shoulder. b) ν_1 = symmetrical stretching of NH_4^+, ν_2 = symmetrical bending of NH_4^+, ν_3 = antisymmetrical stretching of NH_4^+, ν_4 = antisymmetrical bending of NH_4^+, ν_5 = Reststrahlen band of NH_4^+, ν_6 = rotational lattice mode of NH_4^+, ν = stretching, δ = bending, term = terminal, bridg = bridging, a = antisymmetrical, s = symmetrical.

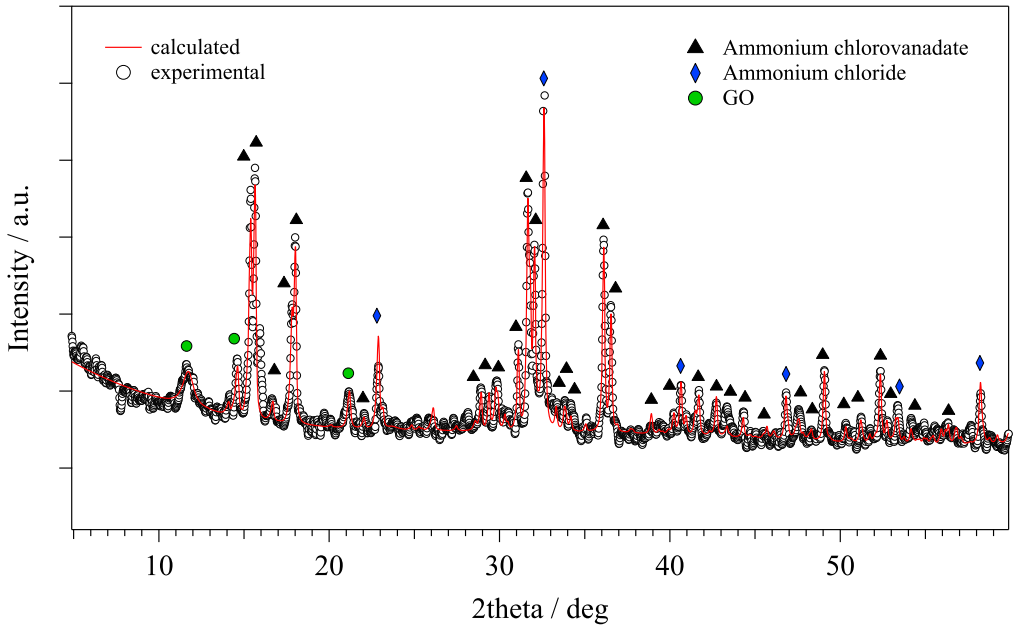

Figure 4. Experimental (black circles) and calculated (red line) powder WAXD patterns of GO@V sample. Peaks of different phases are labeled with different markers: ▲ ammonium chlorovanadate, ♦ ammonium chloride and ● graphene oxide (GO).

vanadium-based nanoparticles, the surface GO nanoflakes and the ammonium interlayer), which are interacting as schematically shown in Fig. 1a. In addition, the WAXD profile obtained after cycling in a battery the material (see Fig. S1 in the supporting information, which is available online at stacks.iop.org/JES/167/070547/mmedia) indicates that the electrochemical reaction of Mg ions with the GO@V cathode induces an amorphization of its active material. Indeed, the only phase that can be detected in the WAXD pattern of the fully discharged GO@V sample is that of graphite (the electron conducting component of the cathodic mixture). Results demonstrate that Mg insertion into V-based nanoparticles acts to disorder this material, reducing its core crystalline phase up to a size below the detection limit of WAXD technique.

Electrochemical studies and battery tests.—Cyclic voltammetry (CV) studies are performed to understand the mechanisms of the electrochemical processes that modulate the insertion and de-insertion processes of Mg^{2+} ions in GO@V material. CV profiles measured at different scan rates are shown in Fig. 5a.

Two different cathodic peaks are observed at ca. 1.0 V (c1), and at ca. 1.8 V (c2). At positive currents, two anodic peaks are revealed, centered at ca. 1.3 V (a1), and 2.2 V (a2). These electrochemical events are highly reversible and occur with a quite low overpotential. In addition to this reduction and oxidation processes of the GO@V material, the oxidation of the electrolyte is also observed at a potential higher than 2.3 V. The electrochemical features of the proposed material are similar to that of pristine V_2O_5.[60] Indeed, the reduction of vanadium species triggers the insertion of magnesium ions into the material in two steps (i.e. at 1.0 V and 1.8 V). This behavior is attributed to a gradual binding of Mg^{2+} ions in two different coordination sites in the crystalline structure of V_2O_5.[60] In the reverse scan of the CV, once both binding sites are completely occupied, magnesium ions are de-inserted giving so rise to two different oxidation current peaks of vanadium-based species at 2.2 and 1.3 V. The insertion and de-insertion processes of Mg^{2+} ions into the cathodic structure is highly reversible and stable in time, despite the significant structural transition occurring during the cycling of the material. The dependence on $v^{1/2}$ (the square root of the scan rate) of the oxidation and reduction current peak values shows a well-defined linear trend, confirming that the insertion/de-insertion processes occur via fast kinetic processes (rapid charge transfer) and with a high reversibility (see Fig. 5b). These electrochemical ex situ studies allowed to demonstrate that the here proposed synthetic protocol is very effective for the preparation of materials which are suitable for the insertion and de-insertion of magnesium ions with a high reversibility and with a fast kinetic process.

Finally, GO@V sample is used to prepare a cathode of a single CR2032 full coin cell, using magnesium metal as anode and an ionic liquid with formula $[EMImCl/(AlCl_3)_{1.5}]/(\delta\text{-}MgCl_2)_{0.08}$ as an electrolyte.[5] This coin cell is cycled from 0.5 to 2.5 V at a current rate of 12.5 C (1000 mA g^{-1}). The galvanostatic charge/discharge polarization curves are shown in Fig. 5c. As expected on the basis of CV measurements, two different plateaus are revealed in the discharge polarization curves (Fig. 5c). The first takes place at ca. 2.20 V, while the second occurs at ca. 1.70 V, and lasts for a longer time. With respect to the electrochemical events detected by ex situ CV measurements, these phenomena in polarization curves are measured at potentials that are slightly higher. Probably, in the coin cell a lower electrolyte overvoltage is observed during the reduction processes, which are likely associated to a smaller distance existing in the battery between the anode and the cathode. Furthermore, during the first discharge the GO@V cathode material delivers a capacity of 72 mAh g^{-1}, even if it is cycled at a very high current rate (1000 mA g^{-1}, i.e. 4.12 mA cm^{-2} corresponding to ca. 12.5 C). This specific capacity is higher with respect to that reported in the literature for V_2O_5 systems tested with completely anhydrous electrolytes.[5,19,61] Pristine V_2O_5 is unable to sustain the applied high current rate. Indeed, when it is cycled under the same conditions as GO@V at 1000 mA g^{-1}, a discharge specific capacity lower than 10 mAh g^{-1} is revealed (Fig. S2 of the Supporting Information). It should be highlighted that GO@V cathodic material is very promising for the extremely high current rate used to cycle it in the coin cell without any significant loss of capacity. In the literature it is typically reported that Mg batteries are cycled between 0.1 and 1.0 C, without exceeding 500 mA g^{-1}.[11,24,62] On the other hand, GO@V sustains a specific power of 1.70 W g^{-1}. This value is higher with respect to that of Mo_6S_8 Chevrel-phase, which today is the state-of-the-art for positive electrodes of magnesium batteries and which, typically, is cycled at a maximum specific power of 0.24 W g^{-1}. It should be observed that the specific power adopted to cycle GO@V is also very promising if compared to that of

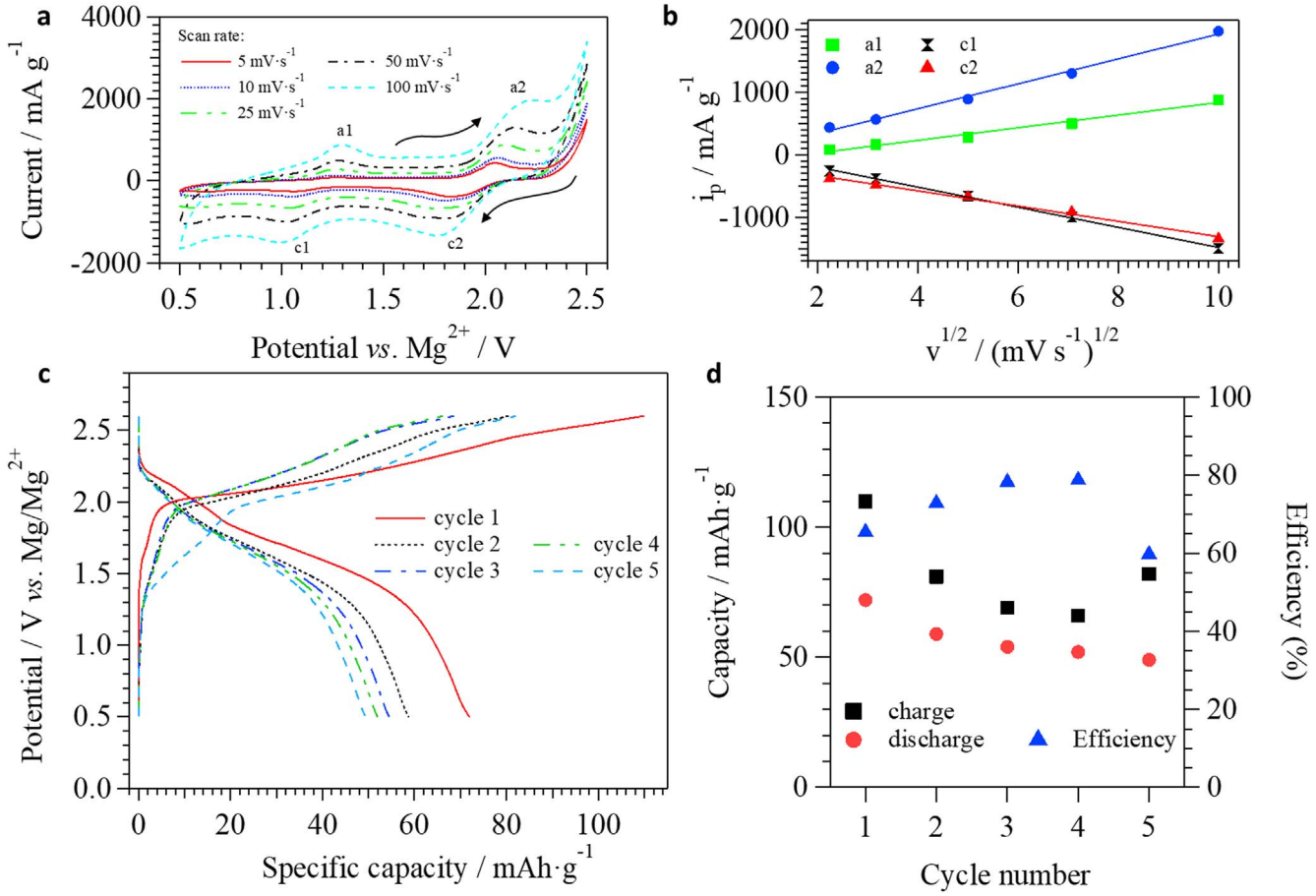

Figure 5. CV curves measured at different scan rates (a). Dependence of the peak current maxima (i_p) of Fig. 5a on the scan rate square root ($v^{1/2}$) (b). Battery test: cycling performance at ca. 12.5 C (1000 mA g^{-1}) of GO@V sample in a CR2032 single cell (c) and charge and discharge capacity and Coulombic efficiency behavior on cycle number (d).

commercially-available cathodes for Li-ion batteries, such as $LiCoO_2$ and $LiFePO_4$. Indeed, $LiCoO_2$ is usually cycled at a specific power in the range 0.05 ÷ 2.50 W g^{-1} (typically 0.52 W g^{-1}), while $LiFePO_4$ shows values in the range 0.06 ÷ 2.80 W g^{-1} (commonly at 0.56 W g^{-1}). The remarkable performance of GO@V, which is correlated to its particular architecture and to the presence of GO flakes strongly interacting with VO_3^- (see Scheme 1b), likely depends on the ability of this cathode to bind large amount of Mg^{2+} ions at the interface between the cathodic material and the electrolyte. This performance is also correlated to the electron charge transfer processes, which in this material are catalyzed by GO component and are also facilitated by the raising of the conductivity of the cathode. The observed capacity fade (Fig. 5d) is reasonably associated to the progressive decomposition of the electrolyte. Indeed, the high current rates and the charging *cut-off* voltage used to cycle the battery overcome the electrochemical stability window of the electrolyte here used in this magnesium battery.[5–7,10,63]

Conclusions

A new high-performing cathode material for magnesium battery applications based on graphene oxide flakes anchored by electrostatic interactions onto the surface of a vanadium-based "*core*" is synthetized by using a combined chemico-electrochemical process. HR-TGA, vibrational and WAXD studies allow to reveal that the obtained material is characterized by a suitable architecture consisting of: a) electrochemically active nanoparticles based on a crosslinked 3D network of oxyvanadyl-chloride and -sulphate species; and b) an ammonium inter-layer able to strongly fix by means of electrostatic interactions a graphene oxide "*shell*" to the vanadium-based *"core"* nanoparticles. Thus, the surface of GO, which is mainly covered by alkoxide functionalities, is neutralized by the bridging NH_4^+ cations. This hypothesized *layer by layer* architecture is confirmed by STEM electron microscopy studies, which reveal the presence of a *chrysalis-like* ordered superstructure where GO is wrapping the V-based nanoparticles "*core*." Moreover, STEM images allow to distinguish that vanadium *"core"* nanoparticles present on their surface ammonium bridges which are responsible for its very porous surface. A CR2032 coin cell battery is assembled and tested by using: a) the here proposed material as the cathode; b) a Mg metal foil as the anode; and c) a $[EMImCl/(AlCl_3)_{1.5}]/(\delta\text{-}MgCl_2)_{0.08}$ ionic liquid as the electrolyte. This coin cell during the first cycle provides a specific capacity of ca. 72 mAh g^{-1}. Taken all together, the most remarkable result here obtained for the proposed material is its very high current rate and specific power during cycling in coin cells. It should be concluded that, for the first time, a cathode for a non-aqueous secondary magnesium battery is cycled at 1000 mA g^{-1} (4.12 mA cm^{-2}, 1.70 W g^{-1}). However, for this type of battery configuration, the development of a more stable electrolyte is mandatory in order to improve its cyclability.

Acknowledgments

This work was supported by the European Union's Horizon 2020 research and innovation program under grant agreement Graphene Core 2 785219, the program "Budget Integrato per la Ricerca Interdipartimentale—BIRD 2018" of the University of Padova (protocol BIRD187913) and by the "Centro Studi di Economia e

Tecnica dell'Energia Giorgio Levi Cases" of the University of Padova. The authors would like to thank Dr. Chuanyu Sun for his technical support.

ORCID

Gioele Pagot https://orcid.org/0000-0002-4015-6670
Keti Vezzù https://orcid.org/0000-0003-4156-7479
Maurizio Fauri https://orcid.org/0000-0003-2162-2055
Andrea Migliori https://orcid.org/0000-0003-4340-4534
Vittorio Morandi https://orcid.org/0000-0002-8533-1540
Enrico Negro https://orcid.org/0000-0002-3340-3899
Vito Di Noto https://orcid.org/0000-0002-8030-6979

References

1. B. Scrosati and J. Garche, *J. Power Sources*, **195**, 2419 (2010).
2. V. Di Noto, S. Lavina, G. A. Giffin, E. Negro, and B. Scrosati, *Electrochim. Acta,*, **57**, 4 (2011).
3. G. Martin, L. Rentsch, M. Höck, and M. Bertau, *Energy Storage Mater.*, **6**, 171 (2017).
4. E. Sheha, *Graphene*, **3**, 36 (2014).
5. F. Bertasi et al., *ChemSusChem*, **8**, 3069 (2015).
6. F. Bertasi, F. Sepehr, G. Pagot, S. J. Paddison, and V. Di Noto, *Adv. Funct. Mater.*, **26**, 4860 (2016).
7. F. Bertasi, K. Vezzù, G. Nawn, G. Pagot, and V. Di Noto, *Electrochim. Acta*, **219**, 152 (2016).
8. V. Di Noto and M. Fauri, *Magnesium-based primary (non-rechargeable) and secondary (rechargeable) batteries* (2000), Publication Number: WO/2001/009972; International Application No.: PCT/EP2000/007221.
9. V. Di Noto, S. Lavina, D. Longo, and M. Vidali, *Electrochim. Acta*, **43**, 1225 (1998).
10. G. Pagot, F. Bertasi, K. Vezzù, F. Sepehr, X. Luo, G. Nawn, E. Negro, S. J. Paddison, and V. D. Noto, *Electrochim. Acta,*, **246**, 914 (2017).
11. I. Shterenberg, M. Salama, Y. Gofer, E. Levi, and D. Aurbach, *MRS Bull.*, **39**, 453 (2014).
12. H. S. Kim, T. S. Arthur, G. D. Allred, J. Zajicek, J. G. Newman, A. E. Rodnyansky, A. G. Oliver, W. C. Boggess, and J. Muldoon, *Nat. Commun.*, **2**, 427 (2011).
13. Z. Zhao-Karger, X. Zhao, O. Fuhr, and M. Fichtner, *RSC Adv.*, **3**, 16330 (2013).
14. O. Tutusaus, R. Mohtadi, T. S. Arthur, F. Mizuno, E. G. Nelson, and Y. V. Sevryugina, *Angew. Chem. Int. Ed.*, **54**, 7900 (2015).
15. V. Di Noto and M. Vittadello, *Solid State Ion.*, **147**, 309 (2002).
16. D. Aurbach, Z. Lu, A. Schechter, Y. Gofer, H. Gizbar, R. Turgeman, Y. Cohen, M. Moshkovich, and E. Levi, *Nature*, **407**, 724 (2000).
17. T. D. Gregory, R. J. Hoffman, and R. C. Winterton, *J. Electrochem. Soc.*, **137**, 775 (1990).
18. G. G. Amatucci, F. Badway, A. Singhal, B. Beaudoin, G. Skandan, T. Bowmer, I. Plitz, N. Pereira, T. Chapman, and R. Jaworski, *J. Electrochem. Soc.*, **148**, A940 (2001).
19. P. Novák and J. Desilvestro, *J. Electrochem. Soc.*, **140**, 140 (1993).
20. Y. Zheng, Y. NuLi, Q. Chen, Y. Wang, J. Yang, and J. Wang, *Electrochim. Acta*, **66** (Supplement C), 75 (2012).
21. K. Makino, Y. Katayama, T. Miura, and T. Kishi, *J. Power Sources*, **112**, 85 (2002).
22. R. Zhang, X. Yu, K.-W. Nam, C. Ling, T. S. Arthur, W. Song, A. M. Knapp, S. N. Ehrlich, X.-Q. Yang, and M. Matsui, *Electrochem. Commun.*, **23** (Supplement C), 110 (2012).
23. H. Tian et al., *Nat. Commun.*, **8**, 14083 (2017).
24. Z. Li, X. Mu, Z. Zhao-Karger, T. Diemant, R. J. Behm, C. Kübel, and M. Fichtner, *Nat. Commun.*, **9**, 5115 (2018).
25. K. V. Kravchyk, R. Widmer, R. Erni, R. J. C. Dubey, F. Krumeich, M. V. Kovalenko, and M. I. Bodnarchuk, *Sci. Rep.*, **9**, 7988 (2019).
26. P. Novák, R. Imhof, and O. Haas, *Electrochim. Acta*, **45**, 351 (1999).
27. Q. An, Y. Li, H. D. Yoo, S. Chen, Q. Ru, L. Mai, and Y. Yao, *Nano Energy*, **18**, 265 (2015).
28. G. Zhao, J. Li, X. Ren, C. Chen, and X. Wang, *Environmental Science & Technology*, **45**, 10454 (2011).
29. L. Lutterotti, M. Bortolotti, G. Ischia, I. Lonardelli, and H. R. Wenk, *Zeitschrift fur Kristallographie, Supplement*, **1**, 125 (2007).
30. V. Di Noto and S. Bresadola, *Macromol. Chem. Phys.*, **197**, 3827 (1996).
31. J. Twu, C.-F. Shih, T.-H. Guo, and K.-H. Chen, *J. Mater. Chem.*, **7**, 2273 (1997).
32. M. Acik, G. Lee, C. Mattevi, M. Chhowalla, K. Cho, and Y. J. Chabal, *Nat. Mater.*, **9**, 840 (2010).
33. T. Szabó, O. Berkesi, and I. Dékány, *Carbon*, **43**, 3186 (2005).
34. T. Szabó, O. Berkesi, P. Forgó, K. Josepovits, Y. Sanakis, D. Petridis, and I. Dékány, *Chem. Mater.*, **18**, 2740 (2006).
35. M. Acik, G. Lee, C. Mattevi, A. Pirkle, R. M. Wallace, M. Chhowalla, K. Cho, and Y. Chabal, *J. Phys. Chem. C*, **115**, 19761 (2011).
36. D. Lin-Vien, N. B. Colthup, W. G. Fateley, and J. G. Grasselli, *The Handbook of Infrared and Raman Characteristic Frequencies of Organic Molecules* (Academic, San Diego) p. 277 (1991).
37. M. R. Todorović, U. B. Mioč, I. Holclajtner-Antunović, and D. Šegan, *Materials Science Forum*, **494**, 351 (2005).
38. K. Nakamoto, *Infrared and Raman Spectra of Inorganic and Coordination Compounds—Part A: Theory and Applications in Inorganic Chemistry* (John Wiley & Sons, INC., Hoboken, New Jersey) p. 427 (2009).
39. R. C. Plumb and D. F. Hornig, *J. Chem. Phys.*, **21**, 366 (1953).
40. R. C. Plumb and D. F. Hornig, *J. Chem. Phys.*, **23**, 947 (1955).
41. W. Vedder and D. F. Hornig, *J. Chem. Phys.*, **35**, 1560 (1961).
42. E. L. Wagner and D. F. Hornig, *J. Chem. Phys.*, **18**, 296 (1950).
43. H. Zhang, T. Kuila, N. H. Kim, D. S. Yu, and J. H. Lee, *Carbon*, **69**, 66 (2014).
44. E. Fuente, J. A. Menéndez, M. A. Díez, D. Suárez, and M. A. Montes-Morán, *J. Phys. Chem. B*, **107**, 6350 (2003).
45. M. Kang, D. H. Lee, J. Yang, Y. M. Kang, and H. Jung, *RSC Adv.*, **5**, 104502 (2015).
46. R. Bariseviciute, J. Ceponkus, and V. Sablinskas, *Cent. Eur. J. Chem.*, **5**, 71 (2006).
47. G. S. Zakharova, C. Täschner, T. Kolb, C. Jähne, A. Leonhardt, B. Büchner, and R. Klingeler, *Dalton Trans.*, **42**, 4897 (2013).
48. N. Kausar, R. Howe, and M. Skyllas-Kazacos, *J. Appl. Electrochem.*, **31**, 1327 (2001).
49. L. Mai and C. Han, *Mater. Lett.*, **62**, 1458 (2008).
50. S. Mohan, S. Gunasekaran, and K. Kumar, *Proc. Indian Natl. Sci. Acad*, **3**, 641 (1986).
51. W. G. Fateley, F. R. Dollish, N. T. McDevitt, and F. F. Bentley, *Infrared and Raman selection rules for Molecular and Lattice Vibrations: the Correlation Method* (Wiley-Interscience, New York, USA) (1972).
52. C. M. Julien, A. Mauger, K. Zaghib, R. Veillette, and H. Groult, *Ionics*, **18**, 625 (2012).
53. G. Pagot, F. Bertasi, G. Nawn, E. Negro, A. Bach Delpeuch, K. Vezzù, D. Cristofori, and V. Di Noto, *Electrochim. Acta,*, **225**, 533 (2017).
54. E. Negro et al., *Electrochim. Acta,*, **280**, 149 (2018).
55. B. Figgis, C. Raston, R. Sharma, and A. White, *Aust. J. Chem.*, **31**, 2717 (1978).
56. G. Bartlett and I. Langmuir, *J. Am. Chem. Soc.*, **43**, 84 (1921).
57. H. C. Schniepp, J.-L. Li, M. J. McAllister, H. Sai, M. Herrera-Alonso, D. H. Adamson, R. K. Prud'homme, R. Car, D. A. Saville, and I. A. Aksay, *The Journal of Physical Chemistry B*, **110**, 8535 (2006).
58. Q. Du, M. Zheng, L. Zhang, Y. Wang, J. Chen, L. Xue, W. Dai, G. Ji, and J. Cao, *Electrochim. Acta*, **55**, 3897 (2010).
59. L. Shahriary and A. A. Athawale, *IJEEE*, **2**, 58 (2014).
60. D. Imamura and M. Miyayama, *Solid State Ion.*, **161**, 173 (2003).
61. L. Yu and X. Zhang, *J. Colloid Interface Sci.*, **278**, 160 (2004).
62. M. Mao, T. Gao, S. Hou, and C. Wang, *Chem. Soc. Rev.*, **47**, 8804 (2018).
63. C. J. Barile, R. G. Nuzzo, and A. A. Gewirth, *J. Phys. Chem. C*, **119**, 13524 (2015).